J. Fluid Mech. (1999), *vol.* 380, *pp.* 205–232. Printed in the United Kingdom

© 1999 Cambridge University Press

Experiments on nonlinear gravity–capillary waves

By LEV SHEMER AND MELAD CHAMESSE

Department of Fluid Mechanics and Heat Transfer, Faculty of Engineering, Tel-Aviv University, Tel-Aviv 69978 Israel

(Received 20 May 1997 and in revised form 31 August 1998)

Benjamin–Feir instability of nonlinear gravity–capillary waves is studied experimentally. The experimental results are compared with computations performed for values of wavelength and steepness identical to those employed in the experiments. The theoretical approach is based on the Zakharov nonlinear equation which is modified here to incorporate weak viscous dissipation. Experiments are performed in a wave flume which has an accurately controlled wavemaker for generation of the carrier wave, as well as an additional independent conical wavemaker for generation of controlled three-dimensional disturbances. The approach adopted in the present experimental investigation allows therefore the determination of the actual boundaries of the instability domain, and not just the most unstable disturbances. Instantaneous surface elevation measurements are performed with capacitance-type wave gauges. Multipoint measurements make it possible to determine the angular dependence of the amplitude of the forced and unforced disturbances, as well as their variation along the tank. The limits of the instability domains obtained experimentally for each set of carrier wave parameters agree favourably with those computed numerically using the model equation. The numerical study shows that application of the Zakharov equation, which is free of the narrow-band approximation adopted in the derivation of the nonlinear Schrödinger (NLS) equation, may lead to qualitatively different results regarding the stability of nonlinear gravity–capillary waves. The present experiments support the results of the numerical investigation.

1. Introduction

Gravity–capillary water waves in the ocean play an important role in the wave energy transfer across the spectrum. Moreover, surface waves in this range are directly responsible for Bragg backscattering of incident electromagnetic waves by the ocean, which is the dominant mechanism for remote sensing of the ocean surface by airborne and spaceborne radars. Of particular interest in this respect is synthetic aperture radar (SAR), which in recent decades has become a major instrument in studies of the ocean surface due to its large coverage, high resolution and independence of weather conditions. The basic principles of SAR imagery of the ocean surface are now well understood (Hasselmann *et al.* 1985). The important parameter which determines the limits of the spatial resolution of SAR images is the so-called scene coherence time (Tucker 1985; Shemer & Marom 1993), which strongly depends on the stability of the resonating backscattering Bragg waves. Detailed knowledge of the stability characteristics of gravity–capillary waves is therefore important in determination of the relative advantages of imaging radars with various electromagnetic wave bands.

https://doi.org/10.1017/S0022112098003620 Published online by Cambridge University Press

The role of gravity–capillary waves in the remote sensing of the ocean surface partially motivated this study. The present investigation, however, is restricted to the stability of those waves due to nonlinear interactions.

For surface gravity–capillary waves, resonant or near-resonant interactions become possible for at least four waves (Class I interactions), although McGoldrick (1965) has shown that for very short ripples, which are strongly affected by surface tension, triad resonant interactions are possible. The particular case of quartet interactions, in which one of the waves (carrier) is taken twice, so that only three waves are actually considered, has attracted much attention. These interactions lead to instability of a monochromatic Stokes wave through sideband disturbances and were theoretically discovered by Benjamin & Feir (1967), although Lighthill (1965) was the first to indicate that a uniform wave train is unstable.

In a seminal paper Zakharov (1968) presented a Hamiltonian description of the water waves problem. The Hamiltonian approach adopted in that study is used as a basis for the stability analysis of surface gravity waves using the nonlinear Schrödinger (NLS) equation. The NLS equation was derived by Zakharov as a particular case of the general integro-differential equation describing the temporal evolution of a four-wave field in Fourier space, the so-called Zakharov equation. The NLS equation, which describes the evolution of nonlinear gravity waves in physical space, is obtained from the Zakharov equation for a narrow wave packet.

Djordjevic & Redekopp (1977) expanded the range of applicability of the NLS equation to shorter gravity–capillary waves. For two-dimensional disturbances, i.e. those propagating in the direction of the carrier, the NLS equation allows one to determine the wavenumber range of the unstable perturbations (Djordjevic & Redekopp 1977; Yuen & Lake 1982). The stability analysis based on the NLS equation performed by Djoerdjevic & Redekopp indicated that there exists a range of wavelengths where gravity–capillary waves are stable to sideband disturbances. The Zakharov equation enables one to study the stability of steady gravity waves of finite amplitude to three-dimensional disturbances (Zakharov 1968; Crawford *et al.* 1981). McLean *et al.* (1981) and McLean (1982) studied this problem by solving numerically the complete governing equations. They uncovered the existence of an additional instability domain, dubbed Class II instability, which results from five waves, or quintet interaction, and is essentially three-dimensional. Class II instability may become dominant at high wave amplitudes. Stiassnie & Shemer (1984) and Shemer & Stiassnie (1985) studied the stability problem using the modified Zakharov equation, extended to the next, fourth, order in wave steepness ϵ, which is the small parameter of the problem. The comparison of the instability domains obtained in these studies with the exact numerical results of McLean *et al.* and McLean for both quartet interaction of Class I (of the order ϵ^3), and quintet interactions of Class II (of the order ϵ^4), indicates that the model is quantitatively correct as long as wave amplitudes do not exceed about one-half of the theoretical maximum. For extremely steep waves, the model becomes less accurate, while still predicting correctly the general qualitative features. Gruman (1987) derived a modification of the Zakharov equation which describes the triad (order ϵ^2) interactions of the capillary and gravity–capillary ripples.

Recently, it was stated that various derivations of the Zakharov equation and its modifications (Zakharov 1968; Yuen & Lake 1982; Stiassnie & Shemer 1984) cannot be rigorously justified (Krasitskii & Kalmykov 1993; Krasitskii 1994; Glozman 1994). Using the Hamiltonian formalism, alternative (and considerably more complicated) model equations were derived in these studies. Although the question regarding the

https://doi.org/10.1017/S0022112098003620 Published online by Cambridge University Press

applicability of the simpler Zakharov equation to the study of the nonlinear dynamics of water waves thus remains open, the aforementioned reasonable quantitative agreement between the results obtained using this equation with the exact computations of McLean indicates that the Zakharov equation can be quite useful for investigations of certain properties of nonlinear water waves. Conclusions regarding the limits of applicability of the Zakharov equation can be drawn, at least partially, by comparing the theoretical predictions obtained by application of this equation with the experimental results.

The first experimental evidence for the existence of third-order resonant interactions was presented by McGoldrick *et al.* (1966). These experiments were restricted to orthogonal wave trains. Benjamin (1967) reported some experimental evidence for the sideband instability due to these interactions. More detailed comparison of the experimental data with the theory of Benjamin & Feir (1967) was performed by Lake & Yuen (1977). The spatial growth of the two sidebands of Benjamin–Feir instabilities of relatively long (of the order of 1 m) steep waves in a basin was observed by Su *et al.* (1982). Melville (1982, 1983) studied experimentally the evolution of unstable steep wave trains and their breaking. His results were in general agreement with Lake & Yuen (1977) and McLean (1982). Theoretical analysis of the stability of very short ripples was carried out by Zhang & Melville (1987), while experiments on triad interactions of short ripples were performed by Henderson & Hammack (1987) and by Perlin, Henderson & Hammack (1990). In these studies, in addition to conventional measurements by wave gauges, a video imaging technique was used to study two-dimensional wave vector spectra. This approach was also applied by Perlin & Hammack (1991) for studies of quartet interactions of gravity–capillary waves.

All theoretical studies of the sideband instability due to the resonant quartet (Class I) interactions indicate that while three-dimensional unstable disturbances exist, the most unstable sideband disturbances for deep gravity surface waves are two-dimensional, i.e. propagate in the direction of the carrier. This is in contrast to the quintet (Class II) interaction, which are strongly three-dimensional (McLean 1982; Stiassnie & Shemer 1984). It should be noted, however, that for short gravity–capillary ripples, the direction of the most unstable sidebands deviates from that of the carrier (Gruman 1987).

In the present investigation we perform a quantitative experimental study of the instability domains of gravity–capillary waves. Measurements are performed for a number of wavelengths and wave steepnesses. The wave-tank study is based on theoretical results obtained by applying the Zakharov equation. In contrast to previous experiments on surface wave instabilities, an artificially controlled disturbance, independent of the carrier, is introduced by an additional wavemaker. It should be stressed that while the theoretical analysis is based on the Hamiltonian approach, water waves observed in any real experiment represent a non-conservative system. To perform a quantitative comparison of the experimental results with the theoretical predictions and to estimate the role of weak dissipation, effects due to water viscosity should be incorporated into the model which originally was derived for potential flow. Viscous damping was recently introduced phenomenologically by Chow, Henderson & Segur (1996) as a correction to a system of ODEs describing a Hamiltonian system which admits three-wave interactions.

The present study is however restricted to longer gravity–capillary waves, for which the lowest possible nonlinear interactions occur for four waves (Class I, or quartet interactions). Ruvinski, Feldstein & Freidman (1986, 1991) presented a derivation of the boundary conditions at the free surface of the potential flow in the presence

https://doi.org/10.1017/S0022112098003620 Published online by Cambridge University Press

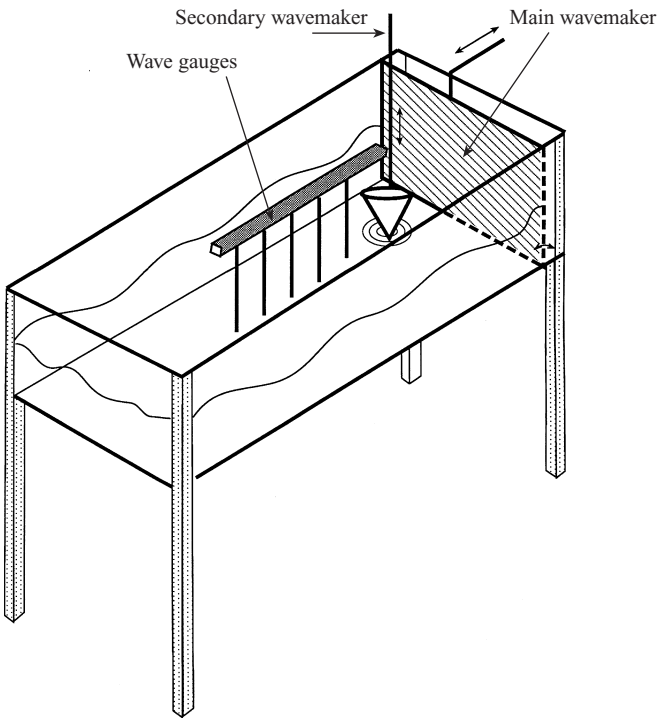


FIGURE 1. The experimental facility.

of weak damping. Longuet-Higgins (1992) corroborated the results of Ruvinski *et al.* using a more straightforward approach. These modified boundary conditions are used in the present study to incorporate weak dissipation quantitatively in the Zakharov equation for various gravity–capillary wavelengths and amplitudes. The resulting equation therefore allows us to estimate the effect of viscosity on the instability domains of weakly nonlinear waves. The instability domains for a number of gravity–capillary wavelengths and amplitudes were computed using the model equation developed. The experiments were then carried out for wave parameters identical to those used in the computations. The quantitative comparison of the theoretically obtained instability domains with the experimental observations enables also an evaluation of the applicability of the Zakharov equation to the study of stability of weakly nonlinear gravity–capillary waves. The additional motivation for the present study is therefore the need for experimental confirmation of the results derived by solving the Zakharov equation.

2. The experimental set-up

The experiments are performed in a flume 1.7 m long, 0.7 m wide and 0.4 m high. A schematic view of the experimental facility is given in figure 1. The flume, supported by a steel frame, has 8 mm thick glass sidewalls, while the bottom is made of 2 cm thick Perspex sheet. The carrier wave is excited by a paddle-type wavemaker located at one end of the tank. The 10 mm thick Perspex paddle spans the tank and is 69.5 cm wide, hinged 5 cm above the tank floor. The gap between the wavemaker and tank walls is 2.5 mm at each side. The wavemaker is driven by a servo-controlled 180 W AC motor. The motor rotation is transferred to the paddle using a 1:4 reducing gear

https://doi.org/10.1017/S0022112098003620 Published online by Cambridge University Press

box and an assembly that has variable eccentricity. The frequency of the carrier wave forcing is stable and can be continuously varied in the range from about 6 to 15 Hz. The frequency range was selected so that the carrier waves were long enough to remove the possibility of resonant triad interactions, yet sufficiently short compared to the size of the experimental facility. The desired wave amplitude can be fixed by varying either the eccentricity of the drive or the water depth in the tank.

In addition to this principal wavemaker, the facility is equipped with an auxiliary wavemaker for the excitation of the sideband disturbances. The auxiliary wavemaker is made of a 10° plastic cone immersed in the water which oscillates vertically, thus producing an axisymmetric wave field. This wavemaker is positioned at least 20 cm from the nearest sidewall and from the principal wavemaker, in order to eliminate the effect of wave reflection. The wavemaker is driven by a separate motor identical to that used for carrier wave production. No reducing gear box is used for the disturbance-generating wavemaker. The supports for both motors and their control units are isolated from the wave flume frame in order to eliminate vibration transfer. A wave absorption device is located at the downstream end of the flume. The secondary wavemaker allows one to excite controlled disturbance with the desired frequency, and thus enables the study of the whole range of the carrier wave instability, and not just the most unstable mode. In addition, the conical shape of the secondary wavemaker allows one to determine experimentally the angular behaviour of the unstable disturbances.

The tank is filled with filtered tap water. The filtering is as follows. First, relatively large solid particles are removed by a 15 μm filter. Organic substances are then removed by an active carbon filter, thus eliminating the possibility of elastic surfactant films on the surface. Finally, fine particles are removed by two additional filters, 1 μm and 0.2 μm. The tank is thoroughly cleaned at the beginning of each set of experiments and fresh water is added. The water depth in the tank is 10–15 cm, satisfying deep water condition for the waves studied in the present experiments. The maximum water depth and wave amplitude are limited by the appearance of cross-waves at the wavemaker excited by parametric resonance at the subharmonic frequency (Kit & Shemer 1989*a*).

The instantaneous surface elevation is measured by one or more capacitance-type wave gauges. The probes were made of 0.6 mm tantalum wire which underwent an anodizing procedure to uniformly coat it with a thin dielectric tantalum oxide layer. The wire coating technology is described in Chapman & Monaldo (1995). The electronic circuitry is based on the design of Chapman & Monaldo, as well. Since their original instrument was aimed at field measurements in the ocean, the electronics are modified considerably to ensure the necessary sensitivity and frequency response, as well as to eliminate cross-talk between the different channels. Up to five wave gauges could be used simultaneously. More details about wave gauges and electronics used in the present study are given in Chamesse (1997).

The effective surface tension in the tank is determined on the basis of the dispersion relation for gravity–capillary waves. Simultaneous measurements of wave frequency and phase velocity are performed, using four wave gauges located at known positions along the tank (Chamesse 1997). The effective value of the surface tension coefficient obtained in these measurements is 70 dynes cm^{-1}. This value of the surface tension coefficient is therefore adopted in the present study.

The gauges are calibrated *in situ* using a stepping motor and a computerized static calibration procedure, as described in detail in Shemer, Kit & Miloh (1987). The calibration is performed at the beginning of each experimental run. Eleven

https://doi.org/10.1017/S0022112098003620 Published online by Cambridge University Press

data points sampled with an increment of 0.4 mm are obtained in the calibration procedure, thus covering the range of ± 2 mm, appropriate for the wave amplitudes encountered in this study, the mean depth of the probe immersion was about 1 cm. For the range of surface elevations observed in this study, the response of the system is found to be linear, and the calibration coefficients are computed for each gauge using the least-squares procedure. To ensure that no variations in the probe response occurred in the course of an experiment, the calibration procedure is repeated after the conclusion of each experimental run. If the new calibration coefficients proved to be notably different from the original ones, the results obtained in this particular run were rejected.

In the present experiments, amplitudes of relatively high-frequency gravity–capillary waves (up to 15 Hz) are measured. To verify the appropriate frequency response of the wave gauges, dynamic calibration is performed. In this procedure, the assembly of the secondary conical wavemaker is employed. The gauges replace the wavemaker cone and are oscillated in the vertical direction with constant amplitude. The wave gauges response as a function of the forcing frequency is found to be flat for all frequencies below about 20 Hz. The low-pass filter of the electronic circuit of the wave gauges is therefore set at 20 Hz. It should be noted that conclusions based on this type of dynamic calibration may not be quite adequate for propagating short waves. The results of a careful investigation by Sturm & Sorrell (1973) who compared the performance of the wire wave gauges with optical measurements indicate that even for the highest wave frequencies studied here, the gauge-measured wave amplitudes remain sufficiently accurate.

Two different types of wave gauge arrangement are employed. In the first type, the gauges are placed on an aluminium bar, where the distance between consecutive sensors could be varied by an increment of about 2.5 cm. The bar, which is parallel to the sidewalls of the tank, is shifted slightly relative to the secondary wavemaker to reduce shadowing effects. Thus, the instantaneous wave elevations could be measured at desired distances from the secondary wavemaker along the carrier wave propagation direction. In the second arrangement, wave gauges are located on a circular arch with a radius of 10 cm, centred at the conical wavemaker. Such distribution of the wave gauges facilitated measurements at a constant distance from the secondary wavemaker and at different angles of propagation of the forced disturbance.

3. Theoretical background

3.1. *Incorporation of weak dissipation into the Zakharov equation*

The irrotational flow of inviscid incompressible deep fluid with free surface at $z = \eta(\boldsymbol{x}, t)$ satisfies the Laplace equation for the velocity potential ϕ

$$\Delta\phi = 0, \quad -\infty < z \leqslant \eta \tag{1}$$

subject to the kinematic

$$\eta_t + \nabla_x \eta \nabla_x \phi - \phi_z = 0, \quad z = \eta \tag{2}$$

and the dynamic

$$\phi_t + \tfrac{1}{2}(\nabla\phi)^2 + gz - s\nabla\left[\frac{\nabla_x \eta}{\left(1 + (\nabla_x \eta)^2\right)^{1/2}}\right] = 0, \quad z = \eta \tag{3}$$

https://doi.org/10.1017/S0022112098003620 Published online by Cambridge University Press

boundary conditions at the free surface. Here s is the surface tension coefficient divided by fluid density, g is the gravitational acceleration, $\boldsymbol{x} = (x, y)$ denotes the horizontal coordinates, z is oriented vertically upwards, $\nabla_x = (\partial/\partial y; \partial/\partial y)$ is the horizontal operator and $\nabla = (\partial/\partial x; \partial/\partial y; \partial/\partial z)$. The dispersion relation for surface gravity–capillary waves is given by

$$\omega^2 = kg + sk^3, \tag{4}$$

where ω is the radian wave frequency and $k = |\boldsymbol{k}|$ is the magnitude of the wave vector. Zakharov (1968) demonstrated that the surface waves problem (1)–(3) allows a Hamiltonian formulation. Using the Hamiltonian approach, Zakharov derived an equation which describes the wave field evolution in Fourier space. The two-dimensional Fourier transform of a function $f(\boldsymbol{x})$ is defined as

$$\hat{f}(\boldsymbol{k}) = \frac{1}{2\pi} \int_{-\infty}^{\infty} f(\boldsymbol{x}) \exp(-\mathrm{i}\boldsymbol{k} \cdot \boldsymbol{x}) \mathrm{d}\boldsymbol{x}. \tag{5}$$

A new complex 'amplitude' is defined that is composed of the amplitude of the surface elevation $\hat{\eta}(\boldsymbol{k}, t)$, and the amplitude of the velocity potential at free surface, $\phi^s(\boldsymbol{x}, t) = \phi(\boldsymbol{x}, z = \eta(\boldsymbol{x}, t), t)$:

$$b(\boldsymbol{k}, t) = \left(\frac{g}{2\omega(\boldsymbol{k})}\right)^{1/2} \hat{\eta}(\boldsymbol{k}, t) + \left(\frac{\omega(\boldsymbol{k})}{2g}\right)^{1/2} \hat{\phi}^s(\boldsymbol{k}, t). \tag{6}$$

The amplitudes $\hat{\eta}(\boldsymbol{k}, t)$, $\hat{\phi}^s(\boldsymbol{k}, t)$ can be easily obtained from the complex amplitude $b(\boldsymbol{k}, t)$ and its complex conjugate (Stiassnie & Shemer 1984). Zakharov utilized the Hamiltonian approach to obtain the evolution equation for the complex amplitude $b(\boldsymbol{k}, t)$. For our purposes, however, an alternative derivation based directly on the governing equations (1)–(3) and suggested by Yuen & Lake (1982) is more suitable. It is assumed that for waves which are sufficiently long so that only quartet (Class I) resonant interactions are possible, the wave field can be decomposed into a dominant, slowly varying in time, component $\tilde{B}$, and a small but rapid bound component B':

$$b(\boldsymbol{k}, t) = \left[\epsilon B_0(\boldsymbol{k}, t_2) + \epsilon^2 B'(\boldsymbol{k}, t, t_2)\right] \exp[-\mathrm{i}\omega(\boldsymbol{k})t], \tag{7}$$

where ϵ is the small parameter of the problem, represented by the steepness of the carrier wave, $\epsilon = k_0\eta(\boldsymbol{k}_0)$, subscript $_0$ denotes the carrier, $\tilde{B}(\boldsymbol{k}, t_2) = O(1)$ and the slow time scale is defined as $t_2 = \epsilon^2 t$. The near-resonant conditions for Class I interactions between four waves are satisfied when

$$\boldsymbol{k}_0 + \boldsymbol{k}_1 - \boldsymbol{k}_2 - \boldsymbol{k}_3 = 0, \quad |\omega_0 + \omega_1 - \omega_2 - \omega_3| \leqslant O(\epsilon^2\omega_0). \tag{8}$$

The Zakharov equation for the slow time evolution of the carrier wave of $\tilde{B} = \epsilon B_0$ is

$$\mathrm{i}\frac{\partial B_0}{\partial t} = \iiint_{-\infty}^{\infty} T^{(2)}_{0,1,2,3} B_1^* B_2 B_3 \delta(\boldsymbol{k}_0 + \boldsymbol{k}_1 - \boldsymbol{k}_2 - \boldsymbol{k}_3) \exp[\mathrm{i}(\omega_0 + \omega_1 - \omega_2 - \omega_3)t] \, \mathrm{d}\boldsymbol{k}_1 \mathrm{d}\boldsymbol{k}_2 \mathrm{d}\boldsymbol{k}_3 \tag{9}$$

where * denotes the complex conjugate, $B_j = B(\boldsymbol{k}_j)$, δ is the Dirac delta function, and $T^{(2)}_{0,1,2,3} = T^{(2)}(\boldsymbol{k}_0, \boldsymbol{k}_1, \boldsymbol{k}_2, \boldsymbol{k}_3)$ is the interaction coefficient which can be found e.g. in Stiassnie & Shemer (1984).

To perform a quantitative comparison of the nonlinear wave stability analysis based on the Zakharov equation (9) with the experimental results, a modification of (9) that takes into account weak viscous wave damping is performed. The assumption of weak dissipation allowed Ruvinsky *et al.* (1986, 1991) to separate the velocity field

https://doi.org/10.1017/S0022112098003620 Published online by Cambridge University Press

into potential and vortical components. As a result of this decomposition of the velocity field, a vortical velocity component V' in the vertical direction appeared in the kinematic boundary condition, with an additional equation for the determination of V'. Longuet-Higgins (1992) suggested a simplification of the model by Ruvinski *et al.* by invoking the boundary layer concept and presenting the surface elevation as

$$\eta = \tilde{\eta} + \eta', \quad \eta' = \int V' \mathrm{d}t. \tag{10}$$

The boundary conditions are now evaluated at the edge of the potential region $\eta = \tilde{\eta}$. The following modification of (2) and (3) is obtained:

$$\tilde{\eta}_t + \nabla_x \tilde{\eta} \nabla_x \phi - \phi_z = 0, \quad z = \tilde{\eta}, \tag{11}$$

$$\phi_t + \tfrac{1}{2}(\nabla\phi)^2 + g\tilde{\eta} - s\nabla\left[\frac{\nabla_x \tilde{\eta}}{\left(1 + (\nabla_x \tilde{\eta})^2\right)^{1/2}}\right] + 4\nu\phi_{zz} = 0, \quad z = \tilde{\eta}, \tag{12}$$

where ν is the kinematic viscosity of the fluid. For the wavelengths and amplitudes considered in the present study, $\epsilon = O(10^{-1})$ and the following relation holds:

$$2\nu k^2 \omega \leqslant O(\epsilon^2). \tag{13}$$

The boundary conditions (11) and (12) can now be employed instead of (2) and (3), respectively, in order to derive a weakly dissipative version of the Zakharov equation (9), following the derivation procedure of Yuen & Lake (1982). Invoking condition (13), the dissipation appears in the resulting equation for the evolution of a nonlinear wave at a slow time scale as an additional linear term:

$$\mathrm{i}\frac{\partial B_0}{\partial t} = \int\int\int_{-\infty}^{\infty} T^{(2)}_{0,1,2,3} B_1^* B_2 B_3 \, \delta(\boldsymbol{k}_0 + \boldsymbol{k}_1 - \boldsymbol{k}_2 - \boldsymbol{k}_3) \times \exp[\mathrm{i}(\omega_0 + \omega_1 - \omega_2 - \omega_3)\, t] \, \mathrm{d}\boldsymbol{k}_1 \mathrm{d}\boldsymbol{k}_2 \mathrm{d}\boldsymbol{k}_3 - 2\mathrm{i}\nu k_0^2 B_0. \tag{14}$$

3.2. *The effect of weak dissipation on the linear stability of a wave train*

Following Stiassnie & Shemer (1984) and Shemer & Stiassnie (1985), we consider a near resonating Class I quartet, consisting of a carrier wave with a wave vector $\boldsymbol{k}_0$ taken twice, and additional waves (sideband disturbances) with the wave vectors $\boldsymbol{k}_1$ and $\boldsymbol{k}_2$, so that $2\boldsymbol{k}_0 = \boldsymbol{k}_1 + \boldsymbol{k}_2$. It is customary to express this three-wave system through the parameters p and q, where

$$\boldsymbol{k}_0 = \boldsymbol{k}_0(1, 0), \quad \boldsymbol{k}_1 = \boldsymbol{k}_0(1 + p, q), \quad \boldsymbol{k}_2 = \boldsymbol{k}_0(1 - p, -q). \tag{15}$$

The amplitudes of the sideband disturbances B_1 and B_2 are assumed to be small, so that

$$\frac{|B_1|}{|B_0|} = O\left(\frac{|B_2|}{|B_0|}\right) = O(\epsilon). \tag{16}$$

The discretized system of governing equations for such a three-wave system can therefore be linearized with respect to B_1 and B_2 and has the following form:

$$\mathrm{i}\frac{\mathrm{d}B_0}{\mathrm{d}t} = T^{(2)}_{0,0,0,0}|B_0|^2 B_0 - 2\mathrm{i}\nu k_0^2 B_0, \tag{17a}$$

$$\mathrm{i}\frac{\mathrm{d}B_1}{\mathrm{d}t} = T^{(2)}_{1,0,1,0}|B_0|^2 B_1 + T^{(2)}_{1,2,0,0} B_2^* B_0^2 \exp[-\mathrm{i}(2\omega_0 - \omega_1 - \omega_2)t] - 2\mathrm{i}\nu k_1^2 B_1, \tag{17b}$$

$$\mathrm{i}\frac{\mathrm{d}B_2}{\mathrm{d}t} = T^{(2)}_{2,0,2,0}|B_0|^2 B_2 + T^{(2)}_{2,1,0,0} B_1^* B_0^2 \exp[-\mathrm{i}(2\omega_0 - \omega_1 - \omega_2)t] - 2\mathrm{i}\nu k_2^2 B_2. \tag{17c}$$

https://doi.org/10.1017/S0022112098003620 Published online by Cambridge University Press

Equation (17*a*) is decoupled from (17*b*) and (17*c*), to the order of approximation adopted here (its solution for sufficiently short times), so that for $\epsilon^2\omega t \ll 1$ it has the following form:

$$B_0(t) = B_0(0)\exp(-\mathrm{i}T^{(2)}_{0,0,0,0}|B_0(0)|^2 t)\exp(-2\nu k_0^2 t) = B_0(0)[(1 + O(\epsilon^2\omega_0 t)]. \tag{18}$$

This allows one to look for the solution of (17*b*, *c*) in the following form:

$$\left.\begin{aligned} B_1(t) &= B_1(0)\exp[-\mathrm{i}(\tfrac{1}{2}\Omega + \delta)t]\exp(-2\nu k_1^2 t), \\ B_2(t) &= B_2(0)\exp[-\mathrm{i}(\tfrac{1}{2}\Omega + \delta)t]\exp(-2\nu k_2^2 t), \end{aligned}\right\} \tag{19}$$

where $\Omega = 2\omega_0 - \omega_1 - \omega_2 + 2T^{(2)}_{0,0,0,0}|B_0(0)|^2$. The value of δ is given by

$$\delta = (T^{(2)}_{1,0,1,0} - T^{(2)}_{2,0,2,0})|B_0(0)|^2 \pm D^{1/2}, \tag{20a}$$

where the discriminant D is

$$D = \left[\Omega - 2(T^{(2)}_{1,0,1,0} - T^{(2)}_{2,0,2,0})|B_0(0)|^2\right]^2 - 4T^{(2)}_{1,2,0,0}T^{(2)}_{2,1,0,0}|B_0(0)|^4. \tag{20b}$$

It follows from (18) and(19) that the growth rate σ_i for the ith disturbance, $i = 1, 2$, is given by

$$\sigma_i = \mathrm{Im}\,(D^{1/2}) - 2\nu k_i^2. \tag{21}$$

The value of the discriminant D for the wave system given by (15) can be calculated for any p and q from (20*b*). These coordinates therefore conventionally serve as the demarcation of instability domains of potential wave trains with $\nu = 0$ (McLean 1982; Stiassnie & Shemer 1984; Gruman 1987). The growth rate σ_i in this case is identical for both sidebands. To check the present computational procedure, the results for the inviscid waves are verified against those published previously, both for the relatively long gravity waves (Stiassnie & Shemer 1984; Shemer & Stiassnie 1985) and for shorter gravity–capillary waves (Gruman 1987). In the presence of weak dissipation, the instability pattern may become quite different from the potential case. A situation is possible in this case where one of the sidebands is unstable, while the companion disturbance with a shorter wave vector decays. Moreover, the location of the most unstable mode may become affected by weak dissipation and does not necessarily correspond to the three-wave system with a minimum in D.

4. Results of the theoretical model

4.1. *Analysis of the instability of gravity–capillary waves*

In order to perform a quantitative experimental study of the sideband instability of Stokes waves, it is necessary to know first the theoretical limits of the domains of instability and the characteristic parameters of the most unstable disturbance. The computations based on the model presented in the previous Section are performed for the whole range of the wavelengths and wave steepness values under consideration. The dependence of the computed maximum growth rate σ_{max} on the wave steepness $\epsilon = a_0 k_0$ is presented in figure 2 for a number of carrier wave frequencies f. In addition to the wave frequencies that are within the range considered in this study, computational results are also graphed for a wave with $f = 1.77\,\mathrm{Hz}$ ($\lambda = 50\,\mathrm{cm}$), which is long enough to represent a gravity wave unaffected by capillarity. To enable comparison of the maximum growth rates for different values of f, the values of σ_{max} in figure 2 are normalized by the corresponding frequencies of the carrier wave. The

https://doi.org/10.1017/S0022112098003620 Published online by Cambridge University Press

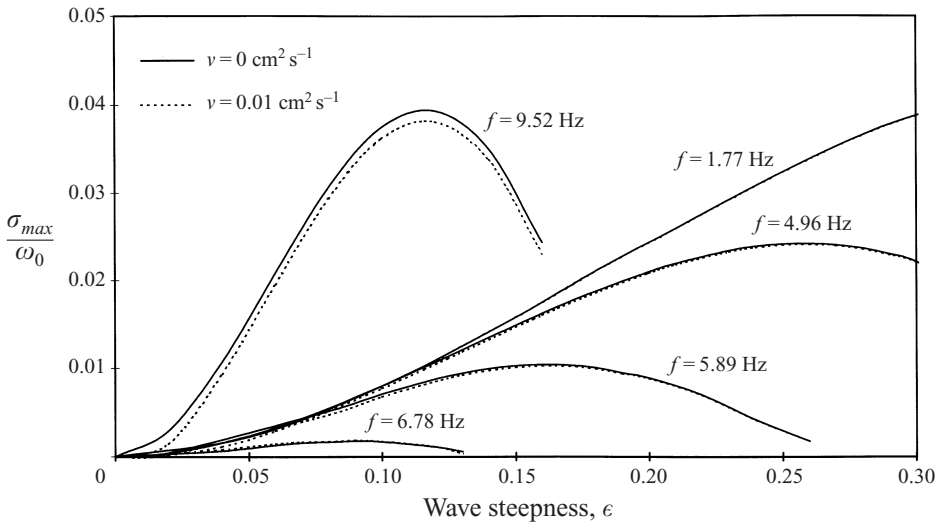


FIGURE 2. The maximum growth rate σ_{max} as a function of the wave steepness ϵ for a number of carrier wave frequencies.

effect of molecular viscosity is obviously more pronounced for the high-frequency sideband, see (21). Maximum growth rates calculated using (21) are therefore plotted in figure 2 both for the potential flow ($v = 0$), where they are identical for both sidebands, and for the high-frequency sideband, in the presence of molecular viscosity ($v = 0.01\,\mathrm{cm^2\,s^{-1}}$). The computation results are presented for $0 < \epsilon < 0.30$. For these values of the carrier wave steepness, good quantitative agreement exists between the model results and the full nonlinear solutions (McLean 1982), see Stiassnie & Shemer (1984).

It is clear from figure 2 that even for the shortest wave considered ($f = 9.52\,\mathrm{Hz}$, $\lambda = 2.5\,\mathrm{cm}$), the maximum growth rate is only weakly affected by molecular dissipation. For longer carrier waves, the viscosity of water can be practically neglected in computations of σ_{max}. It is somewhat surprising that the growth rates of the most unstable disturbances of quite short gravity–capillary waves are only insignificantly modified by dissipation. This can be explained by the fact that the instability growth rates for these waves, even for relatively low values of the carrier wave steepness are substantially larger than the effect of dissipation $2\nu k_i^2$.

Several peculiar features become apparent from observation of figure 2. First, for shorter gravity–capillary carrier waves, the maximum growth rate does not grow monotonically with ϵ. The values of σ_{max}/ω_0 attain their maximum for wave steepness around $\epsilon = 0.1$ for $f = 9.52\,\mathrm{Hz}$ and $f = 6.78\,\mathrm{Hz}$. For longer waves, the value of ϵ where the maximum in the curve is located gradually increases, and for gravity waves, represented by $f = 1.77\,\mathrm{Hz}$ in figure 2, the dependence of the maximum growth rate on the carrier wave steepness becomes monotonic in the wave steepness range considered in this figure. The maximum absolute value of the growth rate is attained for long (gravity) waves at ϵ exceeding 0.3 (cf. Dysthe 1979). Note also that for $f = 1.77\,\mathrm{Hz}$ any difference between the curves computed for the potential flow and for $\nu = 0.01\,\mathrm{cm^2\,s^{-1}}$ practically vanishes.

The results of figure 2 also indicate that for low and moderate values of ϵ, the short gravity–capillary wave with $f = 9.52\,\mathrm{Hz}$ is considerably less stable than the longer waves. It also appears from this figure that for $f = 6.78\,\mathrm{Hz}$, the computed values

https://doi.org/10.1017/S0022112098003620 Published online by Cambridge University Press

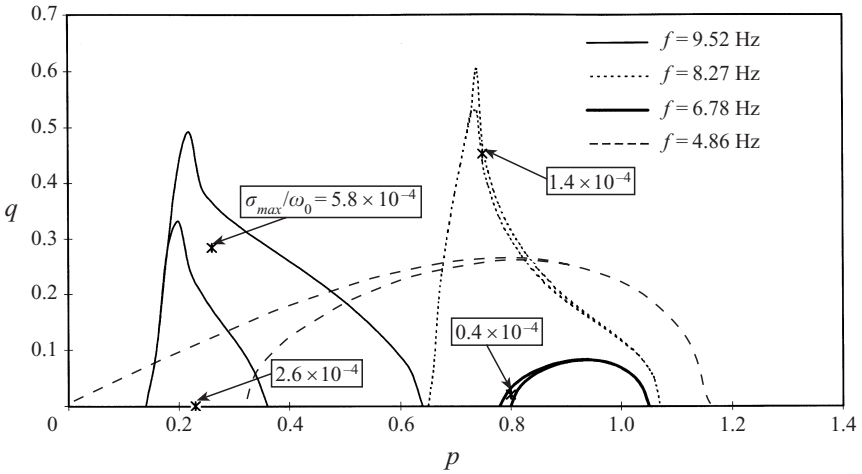


FIGURE 3. The computed instability domains for the wave steepness $\epsilon = 0.1$ (inviscid flow).

of σ_{max}/ω_0 are extremely low. The theoretical model adopted therefore indicates that for this carrier wavelength, the Benjamin–Feir instability actually vanishes. These results are in agreement with the linear stability analysis based on the nonlinear Schrödinger (NLS) equation (Djordjevic & Redekopp 1977). They have shown that gravity–capillary waves are stable for the carrier wavenumber range $k_1 < k < k_2$. Here k_1 corresponds to the minimum of the wave group velocity, i.e.

$$\left.\frac{\partial^2 \omega}{\partial k^2}\right|_{k=k_1} = 0.$$

The short-wavelength limit of the stability domain is determined by the condition $k_2^2 s/g = 0.5$, which corresponds to second order Wilton ripples. In terms of wave frequencies, the NLS equation analysis indicates that waves in the range $6.42 < \lambda < 9.93$ Hz are stable. Note that this range includes the wave frequency $f = 9.52$ Hz, which in the present analysis appears to be unstable, see figure 2. The reasons for this discrepancy are discussed below.

Additional insight into the dependence of the Benjamin–Feir instability on the carrier wave frequency can be obtained from figure 3. The computed instability domains in the (p, q) plane, as defined in (15), are graphed in this figure for various frequencies of gravity–capillary waves with steepness $\epsilon = 0.1$. Since the results of figure 2, as well as some additional computations that were performed, indicate that molecular dissipation is of minor importance to the stability of waves studied here, only waves on the surface of an inviscid fluid are considered in figure 3. Note that the extent of the instability domains varies considerably with f. The instability domain for $f = 4.86$ Hz is similar in shape to that of the Class I instability domains as reported for deep gravity waves in McLean (1982) and Stiassnie & Shemer (1984). The most unstable mode propagates in the direction of the carrier ($q = 0$), The boundary of the instability domain originates at ($p = 0$, $q = 0$), so that there exist unstable disturbances with frequencies approaching that of the carrier wave.

All other graphs of the instability domains in figure 3 represent wavelengths within the domain of stability according to the NLS equation analysis. The results for $f = 6.78$ Hz ($\lambda = 1.0$ cm) and $f = 8.27$ Hz ($\lambda = 3.0$ cm) indicate that instability, albeit very weak, exists for those waves. This minor disagreement between the present

https://doi.org/10.1017/S0022112098003620 Published online by Cambridge University Press

model and the NLS-equation-based results may stem from the fact that a narrow wave spectrum is assumed in the derivation of the NLS equation, while the Zakharov equation is free of this restriction. The weakly unstable disturbances for $f = 8.27$ and $f = 6.78$ Hz indeed have values of $p = O(1)$, so that the wave vectors in the instability domain differ significantly from that of the carrier.

The instability patterns for those waves also change notably, compared to that for $f = 4.86$ Hz. For $f = 6.78$ Hz, the shape of the instability domain still resembles somewhat that of the longer gravity–capillary waves, but the instability is restricted to a very small area in the (p, q)-plane, detached from the origin of the coordinate system, and the most unstable mode no longer propagates exactly in the direction of the carrier ($q = 0$). The vanishing area of the instability domain for $f = 6.78$ Hz explains the extremely low maximum growth rate obtained for this wavelength. For even shorter waves, $f = 8.27$ Hz, the instability domain remains very limited in area, and the growth rate of the most unstable disturbance is still quite low ($\sigma_{max}/\omega_0 = 0.72 \times 10^{-2}$). The shape of this domain is completely unlike that obtained for $f = 6.78$ Hz: it is characterized by relatively large values of q, so that the propagation direction of the unstable disturbances is in this case quite different from that of the carrier wave.

Qualitatively different results are obtained for $f = 9.52$ Hz ($\lambda = 2.5$ cm), still within the range of stable wavelengths according to Djordjevic & Redekopp. The quite strong instability for this wave frequency (cf. figure 2) manifests itself in the area of the instability domain which is considerably larger in this case than for $f = 8.27$ and 6.78 Hz. The instability domain in figure 3 for $f = 9.52$ Hz is detached from the origin in the (p, q)-plane and its shape is somewhat similar to that obtained for $f = 8.27$ Hz. The most unstable disturbances for $f = 9.52$ Hz also propagate at relatively large angle relative to the carrier.

The results of figure 3 are in agreement with Gruman (1987). They indicate that there are two distinct shapes of the instability domains. The gradual transition between shapes occurs in the wave frequency range where gravity–capillary waves are essentially stable. For gravity–capillary waves longer than those in the stability domain, the instability pattern is qualitatively similar to that of gravity waves. For shorter gravity–capillary waves, the sideband instability pattern due to the four-wave interactions becomes quite different. At these wave frequencies, each one of the three waves participating in the nonlinear interaction (the two most unstable sideband disturbances and the carrier) have different directions of propagation. Since the point ($p = 0, q = 0$) does not belong to the instability domain for those waves, there is a finite difference between the frequency of the carrier wave and the range of frequencies of the unstable disturbances.

4.2. *Computed instability domains for the experimental wave parameters*

To enable quantitative comparison of the results of the stability computations with the experiments, it is advantageous to present the computed instability domains separately for each sideband. Convenient coordinates for such a presentation are the propagation angle of the disturbance vs. its frequency. The high-frequency disturbance in our experiments corresponds to the case when the secondary wavemaker excites directly the low-frequency sideband disturbance. We denote these cases as the low-frequency forced experiments. The frequencies $f = \omega/2\pi$ of both disturbances in the analysis are calculated using (4) and (15). The angles of propagation of the high- and the low-frequency disturbances relative to the carrier waves can easily be derived from the known values of (p, q) as $\theta_{1,2} = \tan^{-1}(\pm q/1 \pm p)$, respectively, see (15).

Separate instability domains for the two sidebands are presented in figure 4 for the

https://doi.org/10.1017/S0022112098003620 Published online by Cambridge University Press

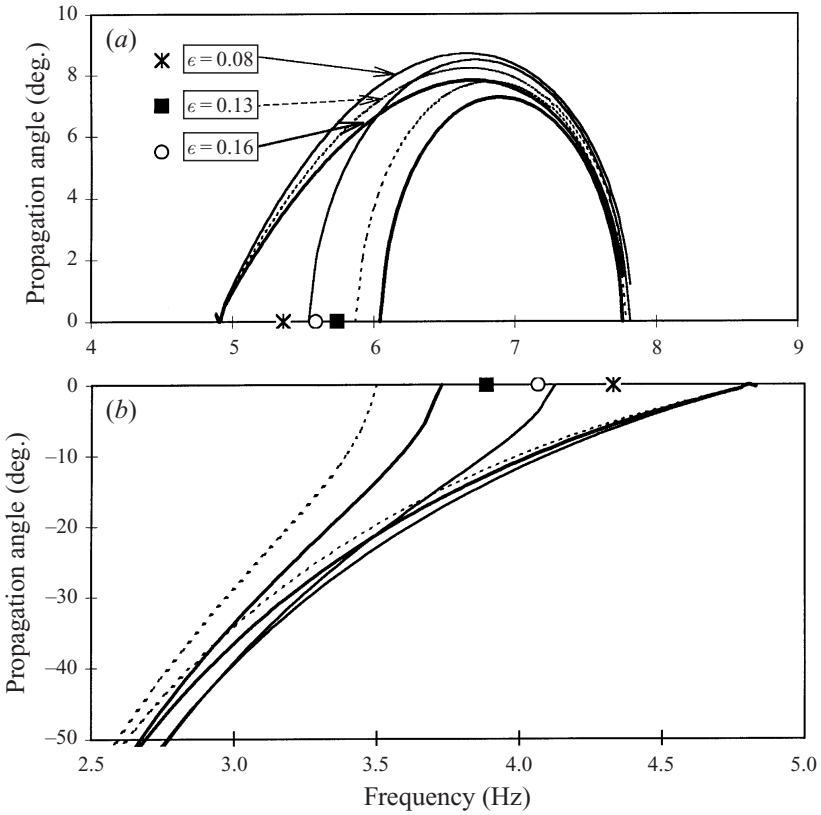


FIGURE 4. The computed (*a*) high and (*b*) low frequency sideband instability domains for the wave frequency $f = 4.86$ Hz. Symbols denote the most unstable mode.

relatively long carrier wave with the frequency of forcing of the principal wavemaker $f = 4.86$ Hz ($\lambda = 7$ cm) and in figure 5 for $f = 5.89$ Hz ($\lambda = 5$ cm). In each figure results of the computations are presented for the values of the carrier wave steepness ϵ for which the experiments were performed. The maximum wave steepness for each wave frequency is restricted in the present experiments by the appearance of cross-waves in the tank.

For all values of ϵ in figures 4 and 5, the most unstable disturbance propagates in the direction of the carrier. The propagation direction of the high-frequency unstable disturbances (figures 4*a* and 5*a*) does not differ from that of the carrier by more than 8° in all cases. In contrast to that, for the low-frequency disturbances the deviation of the propagation direction from that of the carrier can be substantially larger, see figures 4(*b*) and 5(*b*). The domains where low-frequency disturbances are unstable extend to large absolute values of θ, but disturbances with those propagation directions have vanishingly small growth rate. It thus can be concluded that the wave field which can be expected in experiments with sufficiently long carrier waves is essentially two-dimensional.

In general, one of the boundaries of the instability domain in both figures corresponds to the frequency of the carrier wave, and the domains of instability expand as the wave steepness ϵ is increased. A notable exception is obtained for the wave frequency $f = 5.89$ Hz ($\lambda = 5$ cm) and the steepness $\epsilon = 0.16$. For these parameters of the carrier wave, the domains of instability for the high and the low sideband

https://doi.org/10.1017/S0022112098003620 Published online by Cambridge University Press

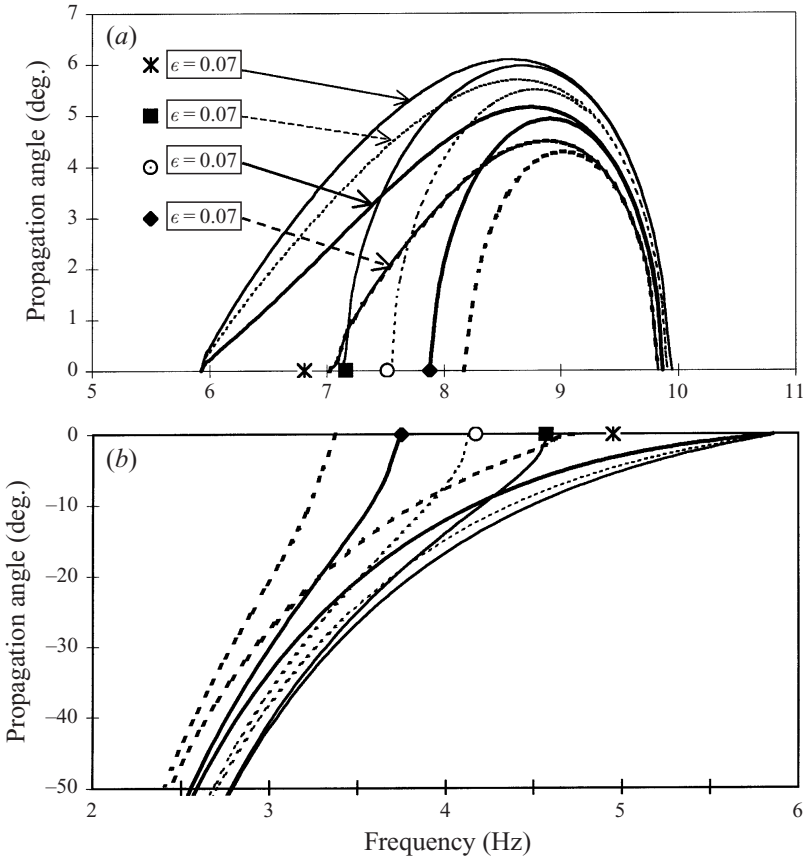


FIGURE 5. As figure 4 but for the wave frequency $f = 5.89$ Hz.

disturbances are detached from the carrier frequency. The value of $\epsilon = 0.16$ is close to the wave steepness for which the maximum is obtained in figure 2. The unstable disturbances for the gravity–capillary waves with high values of wave steepness thus do not satisfy the assumption of the narrow band and have frequencies which are quite different from that of the carrier. It also becomes clear from figure 5 that the decrease in the maximum growth rate with ϵ in figure 2 corresponds to the 'shrinkage' of the instability domains.

Instability domains for three carrier waves frequencies in the range, where they are stable according to Djordjevic & Redekopp (1977) are presented in figure 6 ($f = 6.78$ Hz, $\lambda = 4.0$ cm), figure 7 ($f = 8.27$ Hz, $\lambda = 3.0$ cm) and figure 8 ($f = 9.52$ Hz, $\lambda = 2.5$ cm). The results in figures 6 and 7 are presented for three values of the wave steepness. For $f = 6.78$ Hz, the computations were also performed for larger values of ϵ but the domains of instability at those carrier wave amplitudes actually disappear. In contrast to figures 4 and 5, the instability domains in figures 6 and 7 for different values of ϵ do not overlap, and move away from the carrier forcing frequency with increasing carrier wave steepness. In comparison with the results of figures 4 and 5, the domains of instability in figures 6 and 7 are quite small. The instability exists for an extremely narrow range of frequencies and propagation angles. These results are in agreement with those of figure 2, which show that for $f = 6.78$ Hz the growth rates of the most unstable disturbances are also extremely low. Although the most unstable

https://doi.org/10.1017/S0022112098003620 Published online by Cambridge University Press

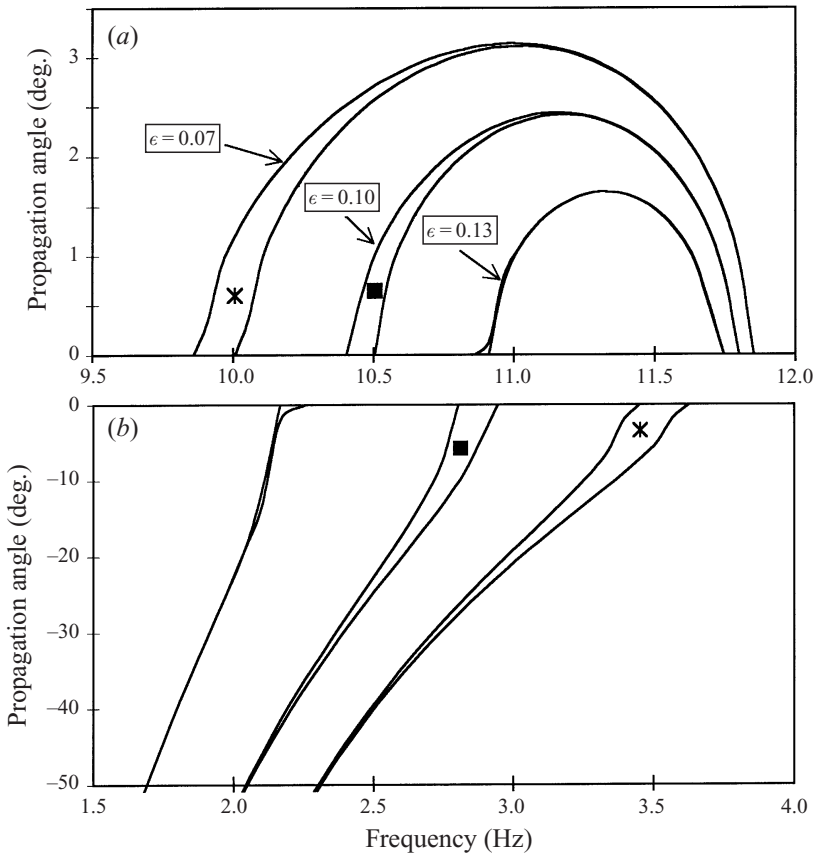


FIGURE 6. As figure 4 but for the wave frequency $f = 6.78$ Hz.

disturbances in figure 6 do not propagate exactly in the direction of the carrier, as is the case for the longer waves, the range of propagation angles of the unstable disturbances is also limited. In contrast to that, the propagation directions of the most unstable disturbances in figure 7, $f = 8.27$ Hz deviate considerably from that of the carrier wave. Note also that while in both figures 6 and 7 the instability domains are nearly vanishing, their shapes in these two figures are quite different. In figure 6, the general shape of the instability domains still resembles that obtained in figure 4 and 5 for longer gravity–capillary waves. As in figure 5 ($f = 5.89$ Hz) for the wave steepness $\epsilon = 0.16$, the assumption of the narrow spectrum is not satisfied in figure 6, and the instability domains are detached from the frequency of the carrier wave. The same conclusion holds for figure 7, but here shape of the instability domains changes notably.

The results of computations of the instability domains for the shorter gravity–capillary waves ($f = 9.52$ Hz, $\lambda = 2.5$ cm), presented in figure 8, look quite different from those plotted in figures 4–6, but strongly resemble in shape those of figure 7. As in figures 6 and 7, the assumption of the narrow spectrum does not hold for this carrier wave frequency. Unlike figure 7, however, the instability domains in figure 8 are quite wide. This is in agreement with figure 2, which indicates that carrier waves with $f = 9.52$ Hz are quite unstable. The computations in figure 8 were performed for the wave steepness $\epsilon = 0.065$, for which the experiments were carried out. In addition, results are shown for $\epsilon = 0.10, \epsilon = 0.13$, corresponding to the maximum in the curve $\sigma_{max}(\epsilon)$ in figure 2, and for a slightly higher value of the wave steepness, $\epsilon = 0.14$. No

https://doi.org/10.1017/S0022112098003620 Published online by Cambridge University Press

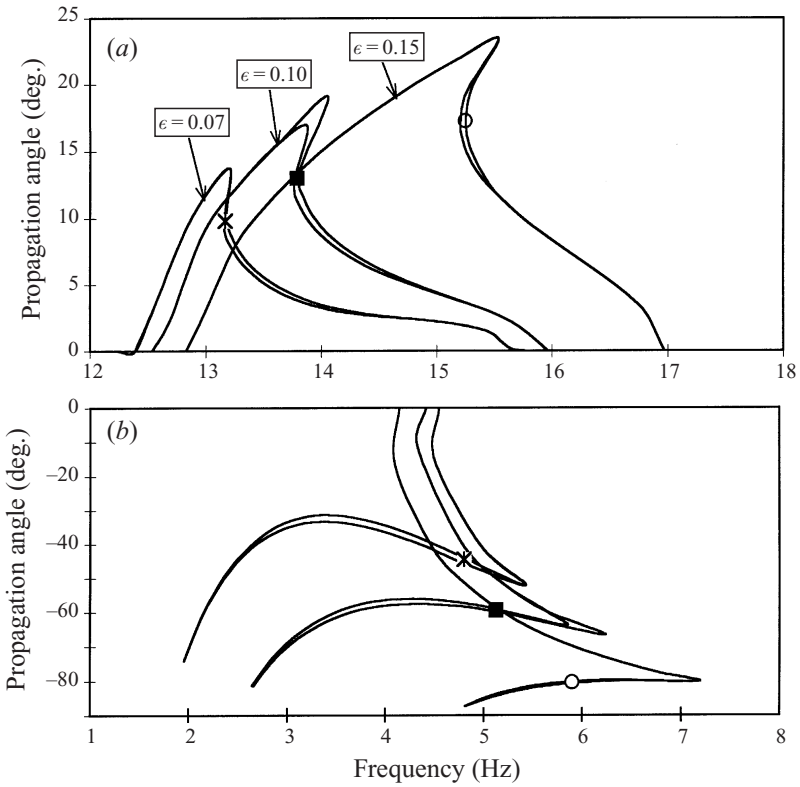


FIGURE 7. As figure 4 but for the wave frequency $f = 8.27$ Hz.

experiments were performed for those relatively high values of ϵ due to appearance of cross-waves in the tank. The most unstable disturbances at both the high frequency and the low frequency propagate at notable angles relative to the carrier. In this case, the wave vector of the most unstable disturbance of the high-frequency sideband has an angle $\theta \approx 10^\circ$ relative to $\boldsymbol{k}_0$, while for the low-frequency sideband θ is about -20°. These results are again in agreement with Gruman (1987). For $f = 9.52$ Hz, one can therefore expect to observe in the experiments a three-dimensional wave field, with the sideband disturbances propagating in directions different from that of the carrier. Note also that the instability domains, as well as the locations of the most unstable disturbances, are nearly identical for $\epsilon = 0.10$ and $\epsilon = 0.13$. This fact may be related to the result of figure 2 that for $f = 9.52$ Hz, the growth rates of the most unstable disturbances are also very similar for those values of the wave steepness. For slightly higher value, $\epsilon = 0.14$, the instability domain 'shrinks' in figure 8 again. As was the case in figure 5 for $\epsilon = 0.16$, this phenomenon can be related to the fact that for $f = 9.52$ Hz, this value of the wave steepness corresponds to the growth rate of the most unstable disturbance which is beyond the maximum.

5. Experimental results

It is assumed in the theoretical model adopted that dissipation occurs in the boundary layer at the water–air interface due to molecular viscosity. This dissipation rate is proportional to the liquid viscosity ν. The temporal decay rate is given by $2\nu k^2$, see (14). The corresponding spatial rate of loss of amplitude is given $2\nu k^2/C_g$, where

https://doi.org/10.1017/S0022112098003620 Published online by Cambridge University Press

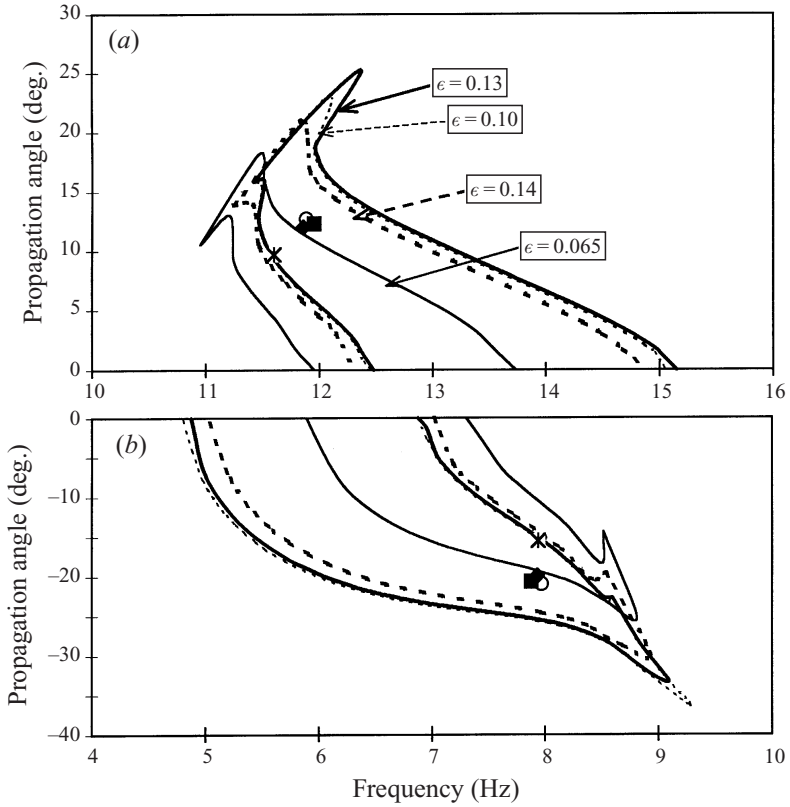


FIGURE 8. As figure 4 but for the wave frequency $f = 9.52$ Hz.

C_g is the wave group velocity (see e.g. Crapper 1984). To verify that this expression holds for the present experimental conditions, measurements of the wave amplitude decay along the tank were performed. The variation of the wave amplitude along the tank demonstrated that the effective value of the kinematic viscosity, estimated from the measured rate of decay, is about 1.5 times larger than that of clean water. This result can be explained by in part by residual contamination of the water surface. Calculations of the dissipation rate due boundary layers at the sidewalls and the bottom of the tank performed using the expressions of Kit & Shemer (1989*b*) indicate that these mechanisms are negligible compared to the molecular dissipation in the boundary layer at the free surface for the wave tank geometry and the wavelengths considered in this study.

The low-pass filtering of the wave gauge outputs at 20 Hz employed in the present studies eliminated the appearance of both parasitic capillary waves (Longuet-Higgins 1995) and Wilton ripples in the recorded signals. It should be stressed, however, that the high-frequency ripples were not observed visually in the tank away from the wavemaker at the locations were the probes are placed. No experiments were performed at carrier frequencies in the close vicinity of the second and the third order internal Wilton resonances.

5.1. *The experimental procedure*

In the experimental approach adopted in the present study, for each value of the frequency of the forced disturbance, amplitudes of the carrier wave and the sideband

https://doi.org/10.1017/S0022112098003620 Published online by Cambridge University Press

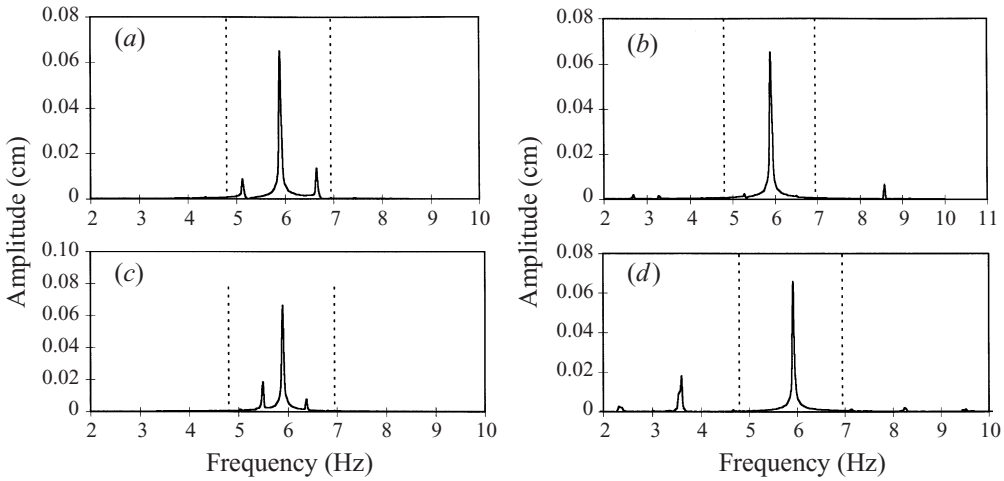


FIGURE 9. Typical measured spectra of the wave field for $f = 5.89$ Hz and $\epsilon = 0.08$: (a, b) high-frequency forced disturbances; (c, d) low-frequency forced disturbance.

disturbances are determined from the measured spectra of the instantaneous surface elevation. The duration of continuous sampling in each experimental run was 80 s, at a sampling frequency of 100 Hz per channel. The calibration coefficients for each wave gauge are determined before each series of measurements, so that actual instantaneous surface elevations at each gauge location could be computed and recorded for further processing. The frequency spectra of the variation of the measured surface elevations with time are then computed by applying the FFT procedure. The spectra for each location have a frequency resolution of about 0.03 Hz. At the beginning of each series of experiments for the desired carrier wave frequency and amplitude, the secondary conical wavemaker is removed, and the resulting wave field is measured when only the principal wavemaker is operating. The exact value of the carrier wave frequency is determined experimentally from the resulting spectra. The wave amplitude at the forcing frequency measured by the wave gauge closest to the secondary wavemaker (at a distance of about 10 cm from the centre off the cone) is used to determine the actual wave steepness in the particular series of experiments. The secondary wavemaker is then inserted, and the measurements are repeated for various frequencies of the forced disturbance. The next sampling is not begun until at least 90 s after the change in wave conditions.

Two types of measurements are performed for the selected values of the carrier wavelength and wave steepness. In the first series of experiments, the variation of the wave field along the tank is studied while in the second series the wave gauges are placed on an arc of radius of about 10 cm centred at the secondary wavemaker. Hence, the resulting wave field is measured as a function of the propagation direction θ of the forced disturbance relative to that of the carrier.

5.2. *Instability domains in the direction of propagation of the carrier wave*

Typical measured wave amplitude spectra representing various situations encountered in the experiments are presented in figure 9. The principal wavemaker operates at the frequency $f = 5.89$ Hz, corresponding to a wavelength of 5.0 cm. The spectra of figure 9 clearly show that in the present experiments three distinct components can easily be identified. The amplitude of each wave component can be estimated

https://doi.org/10.1017/S0022112098003620 Published online by Cambridge University Press

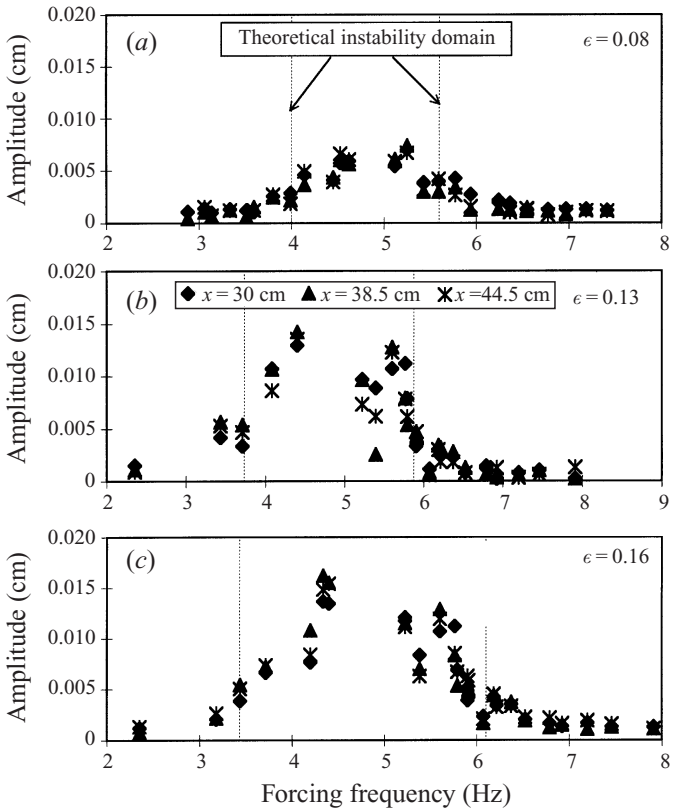


FIGURE 10. The amplitudes of the unforced sideband disturbance measured along the tank for $f = 4.86$ Hz.

from these spectra. The actual amplitudes are calculated by integrating the measured power spectra over five spectral bins centred at the corresponding spectral peak. The carrier wave steepness estimated from the measured spectra is $\epsilon = 0.08$. In figure 9(a, b) the secondary wavemaker excites waves directly at a frequency exceeding that of the carrier (high-frequency forced disturbance), while in figure 9(c, d) low-frequency disturbances are excited directly. In figure 9(a, c) the unforced sideband disturbances are clearly seen in the spectra, thus indicating that nonlinear quartet interactions are present for these experimental conditions. When the secondary wavemaker operates beyond the domain of instability (figure 9b, d) the unforced disturbances are notably weaker. It should be stressed in this respect that the present experimental procedure does not distinguish between the bound and the free waves at a given frequency. The weak peaks beyond the instability domain can therefore be attributed to the presence of the bound waves.

While the carrier wave amplitude, as well as that of the forced disturbance, are affected by the nonlinear interactions, the most dramatic evidence of the presence of instability, from figure 9, is the appearance of a noticeable spectral peak at the frequency corresponding to the unforced sideband. It was therefore decided to present the results of the experimental study as the measured amplitude of the unforced sideband vs. the frequency of the forced disturbance. That is, in the figures that follow, the abscissa represents the forced frequency of the conical wavemaker, while the ordinate is the response of the wave field at the unforced sideband frequency.

https://doi.org/10.1017/S0022112098003620 Published online by Cambridge University Press

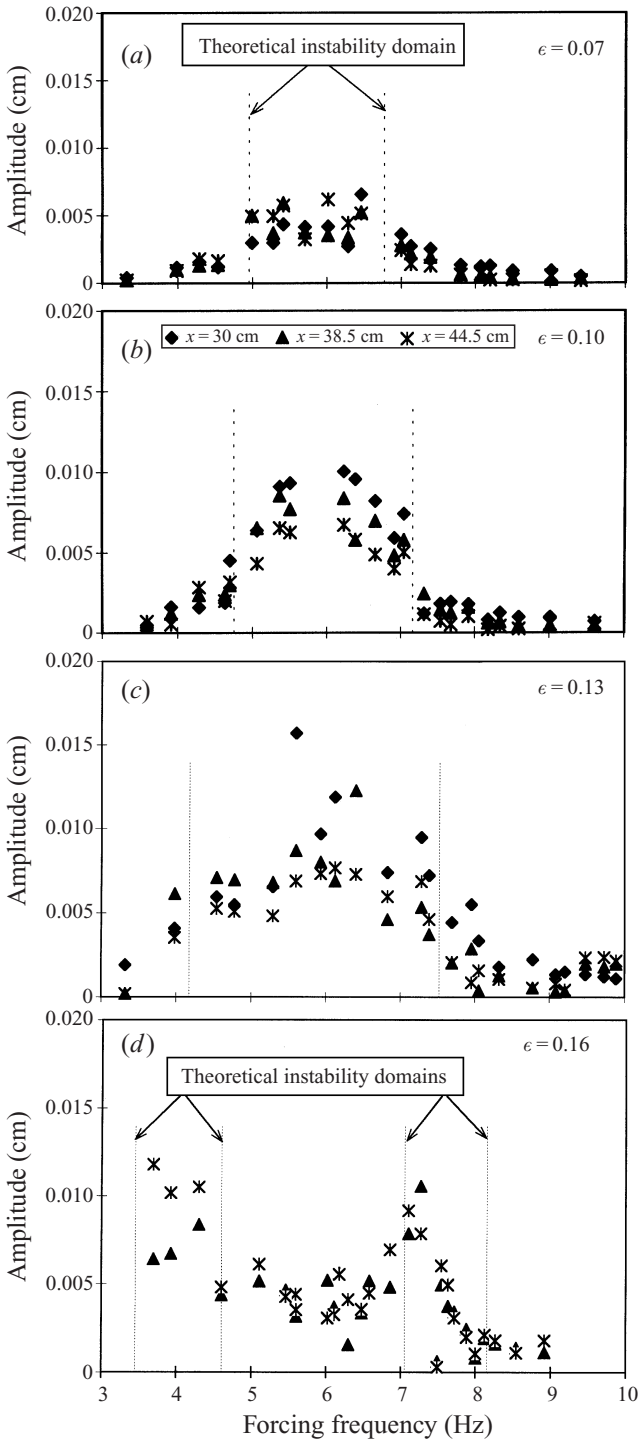


FIGURE 11. As figure 10 but for $f = 5.89$ Hz.

https://doi.org/10.1017/S0022112098003620 Published online by Cambridge University Press

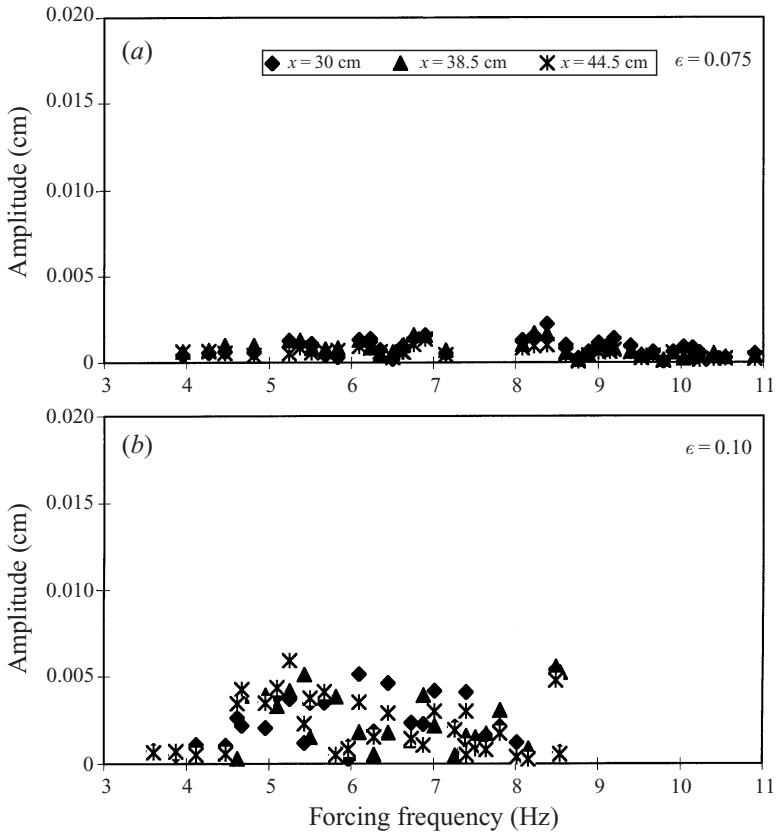


FIGURE 12. As figure 10 but for $f = 6.78$ Hz.

Determination of the instability domains in the direction of the carrier wave propagation is performed using three wave gauges located 30, 38.5 and 44.5 cm from the principal wavemaker. The results obtained at the two carrier wave frequencies ($f = 4.86$ Hz, $\lambda = 7.0$ cm and $f = 5.89$ Hz, $\lambda = 5.0$ cm) are presented in figures 10 and 11, respectively. For $f = 4.86$ Hz, measurements were performed for three carrier wave amplitudes, corresponding to the instability domains computations of figure 4. For shorter gravity–capillary waves with $f = 5.89$ Hz, experimental results are presented in figure 11 for four values of ϵ, including the relatively high value, $\epsilon = 0.16$, where qualitative differences in the instability patterns are obtained in numerical computations compared to the lower values of the carrier wave steepness.

In figures 10 and 11, the range of frequencies is delineated for which the theoretical analysis indicates that disturbances propagating in the carrier direction are unstable. The measured amplitudes of the unforced disturbance within the instability domains predicted by the inviscid theoretical model are consistently notably higher than those outside the theoretical instability limits. The agreement between the experiment and the theory in those figures is both qualitative and quantitative. The effect of widening the instability domains by increasing the steepness of the carrier wave (cf. figures 4 and 5) is clearly observed also in the experiments. Moreover, the limits of the instability as derived from the measured amplitudes of the unforced disturbance are in good agreement with the theoretical predictions for all carrier wave amplitudes at both wavelengths. Fig 11d clearly shows that the measured amplitudes of the unforced

https://doi.org/10.1017/S0022112098003620 Published online by Cambridge University Press

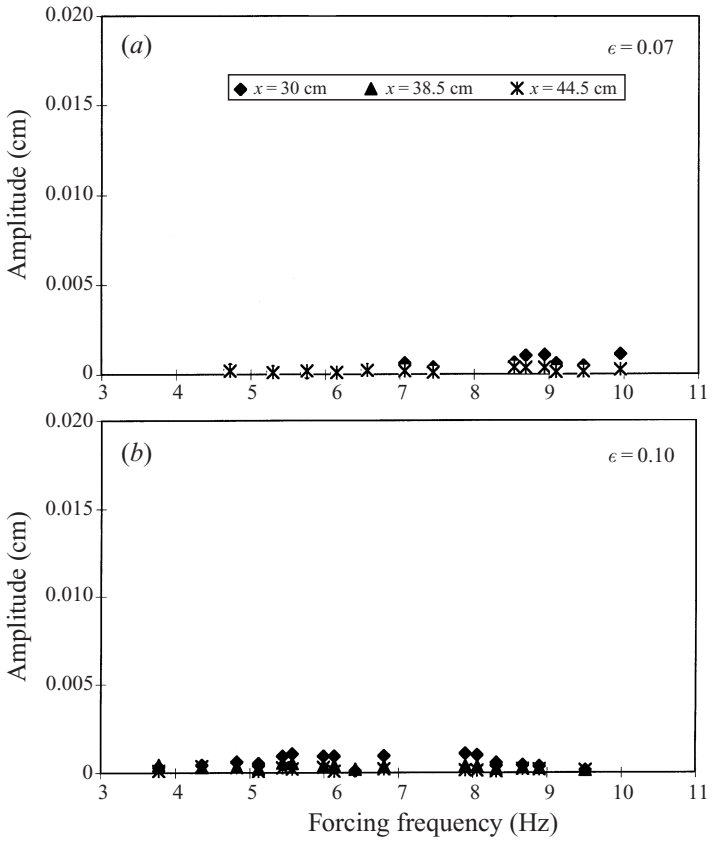


FIGURE 13. As figure 10 but for $f = 8.27$ Hz.

disturbances indeed increase notably in the two detached domains, in agreement with computations for $\epsilon = 0.16$ presented in figure 5.

Results of similar experiments performed for the carrier wave frequencies $f = 6.78$ Hz, $\lambda = 4.0$ cm and $f = 8.27$ Hz, $\lambda = 3.0$ cm are presented in figures 12 and 13, respectively. For each carrier wave frequency, the results are obtained for two carrier wave amplitudes. At the lower amplitude of the carrier wave for $f = 6.78$ Hz ($\epsilon = 0.075$, figure 12*a*), the amplitudes of the unforced disturbance remain vanishingly low. This is in agreement with the theoretical predictions of figure 2 and 7, which suggest that the instability for this carrier wave frequency is very weak. The theoretical computations, however, predict that the instability becomes even weaker until it fades out completely when the amplitude of the carrier is increased. The experimental results obtained for $\epsilon = 0.13$ (figure 12*b*) are somewhat ambiguous. While the measured amplitudes of the unforced disturbance are often notably higher than in figure 12*a*, they are still well below the values obtained for the similar carrier wave steepness for the wave frequency $f = 5.89$ Hz, figure 10*c*. This partial disagreement between the experiments and the theoretical predictions may be plausibly explained by the appearance of bound waves in the spectrum. Results of figure 13 ($f = 8.27$ Hz) are more clear-cut, indicating that no instability is present at this carrier wavelength for both values of the wave steepness ϵ, in full agreement with the predictions of the theoretical model.

https://doi.org/10.1017/S0022112098003620 Published online by Cambridge University Press

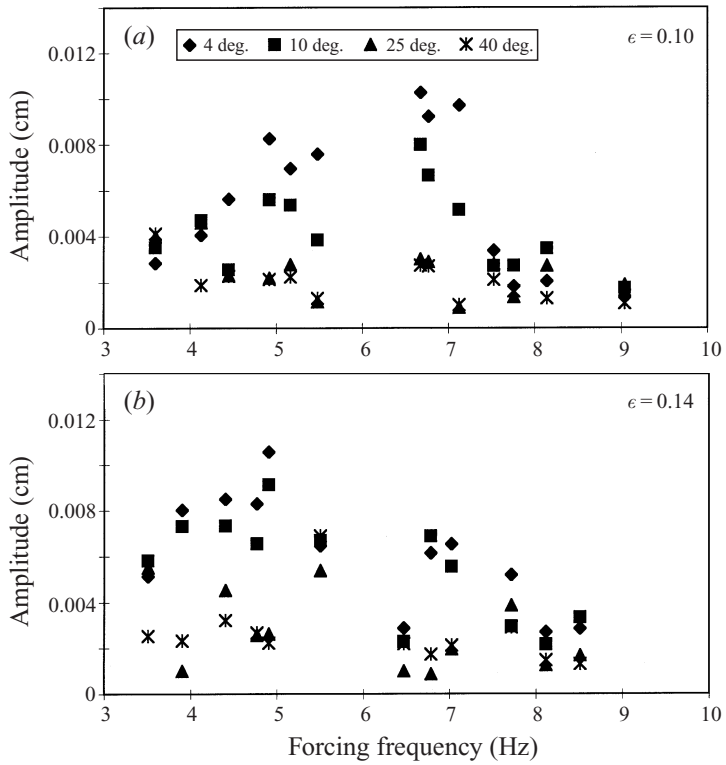


FIGURE 14. Angular dependence of the measured amplitudes of the unforced sideband disturbance for $f = 4.86$ Hz.

5.3. *The angular behaviour of the instability domains*

The dependence of the gravity–capillary waves instability on the angle of propagation of the forced disturbance is studied in figure 14 for $f = 4.86$ Hz and figure 15 for $f = 5.89$ Hz. In each figure, results are presented for two values of the wave steepness. In figure 14*a* ($\epsilon = 0.10$), for all forcing frequencies above about 4.5 Hz, the amplitudes recorded by probe 1, aligned with the carrier wave propagation direction, exceed those at other locations. Note that the theoretical results of figure 5 indicate that, for the carrier wave frequency $f = 5.89$ Hz and steepness $\epsilon = 0.10$, the forced disturbances at those frequencies propagating in the directions of the carrier are indeed unstable. At lower forced disturbance frequencies, only sidebands propagating at angles deviating significantly from that of the carrier can participate in the nonlinear quartet interactions. For those frequencies, the results of figure 14*a* indicate that the unforced disturbance amplitudes measured by the probes positioned away from the carrier wave propagation direction become higher than those recorded by the first probe. At higher carrier wave amplitude, corresponding to $\epsilon = 0.14$, figure 14*b*, the unforced disturbance amplitudes at the first probe location remain larger than those measured by the other probes for all frequencies above about 4 Hz. This trend is again in agreement with the theoretical predictions of figure 5, where the lower boundary of the instability domain for the zero propagation angle is shifted to lower frequencies compared to $\epsilon = 0.10$

Similar qualitative and quantitative agreement between the computed instability domains and the experimental results is observed for both amplitudes for the wave

https://doi.org/10.1017/S0022112098003620 Published online by Cambridge University Press

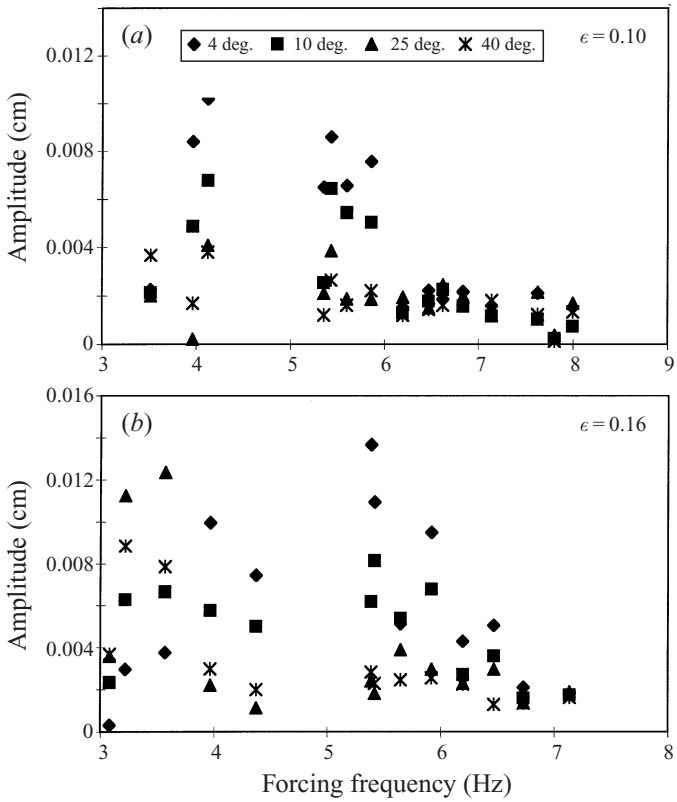


FIGURE 15. As figure 14 but for $f = 5.89$ Hz.

frequency $f = 4.86$ Hz (figure 15). Here again, at all frequencies of the forced disturbance within the domain of instability (approximately $4 < f < 6$ Hz), the amplitudes of the unforced sideband are maximum at the first probe location for $f > 6$ Hz, the results of figure 4 indicate that instabilities propagating at small angles relative to the carrier are still unstable. The domain of instability becomes very narrow and the instability effectively disappears for frequencies exceeding approximately 6.5 Hz. The experimental results of figure 15 are in general agreement with these theoretical calculations. When the conical wavemaker is operating at frequencies below about 3.6 Hz, the measured amplitudes in the direction of the carrier become notably lower than at those in the alternative directions, as can be expected from figure 4.

Experiments on the shortest wave in the present study ($f = 9.52$ Hz, $\lambda = 2.5$ cm) were particularly difficult to perform, mainly due to two complicating factors. First, at this high frequency of forcing subharmonic cross-waves appeared at the wavemaker at a relatively low amplitude of the wavemaker displacement. The largest amplitude of the carrier wave which could be obtained without cross-waves distorting the wave field corresponds to the wave steepness $\epsilon = 0.065$. The absolute values of the surface displacement for these values of ϵ and f are very low. Second, these short waves decay rapidly along the tank, and since the amplitudes are so small even close to the wavemaker, no meaningful measurements were performed along the tank for this carrier wavelength. Experiments therefore were carried out only as a function of the angle of propagation of the disturbances.

https://doi.org/10.1017/S0022112098003620 Published online by Cambridge University Press

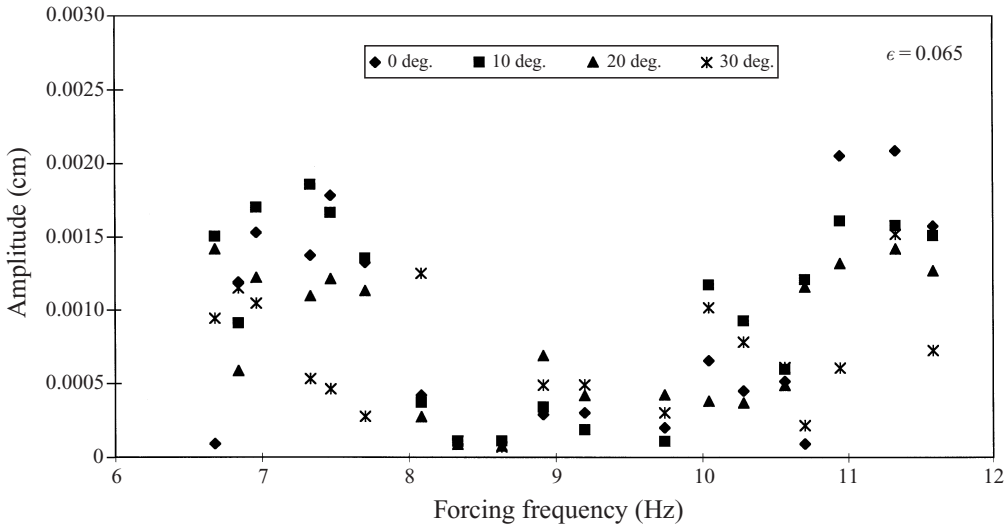


FIGURE 16. As figure 14 but for $f = 9.52$ Hz.

The results of these experiments are summarized in figure 16. The absolute values of the amplitudes of the unforced disturbance in this figure do not exceed 0.025 mm. It should be stressed, however, that relative to the amplitude of the carrier, the wave steepness of the unstable disturbances in figure 16 is higher that those measured for the longer carrier waves. The results of figure 16 support in general the theoretical predictions. The instability domains as obtained in these experiments are detached from the carrier frequency. Moreover, the results of figure 16 indicate that the unforced disturbances measured in the propagation directions of the forced disturbance different from that of the carrier are relatively stronger than those measured at lower carrier frequencies, in particular for the low frequencies of the forced disturbance. These results confirm qualitatively the model predictions presented in figure 8. Due to very small amplitudes in these experiments, it is pointless to consider quantitative agreement.

6. Concluding remarks

The purpose of the present study is to perform an extensive quantitative examination of the Benjamin–Feir instability patterns of weakly nonlinear gravity–capillary waves. This study combines the theoretical analysis of the linear stability of these waves to the sideband disturbances with a corresponding experimental investigation of this problem. The present study is unlike the previous investigations of the instability of the surface waves in two important aspects.

First, a different experimental approach is adopted here. In most experiments on surface wave instability, a carrier wave is generated directly by mechanical means, and the spatial growth of the most unstable disturbances originating from the background noise is then estimated. In contrast to those studies, in the present experiments a controlled omni-directional sideband disturbance is excited directly by an independent wavemaker. The spectra of the surface elevation are then obtained. The presence of an observable second sideband disturbance in these spectra, which is not excited directly, serves as a criterion for the existence of four-wave nonlinear interactions. This experimental procedure allows one to determine not only the most unstable

https://doi.org/10.1017/S0022112098003620 Published online by Cambridge University Press

disturbance, as in other experimental studies, but also to delineate the instability domains.

Secondly, theoretical computations in this work are performed in parallel with the experiments. This approach allows the selection of the experimental parameters for which the measurements are preformed on the basis of the results of the theoretical model adopted. This model is based on the Zakharov integro-differential equation, which describes nonlinear four-wave interactions in the wave-vector space. The model equation is modified to include weak dissipation due to the viscous boundary layer at the free surface in the presence of molecular viscosity. Both quantitative and qualitative comparison is performed between the experimental results and the numerical solution of the model equations.

The present study includes weakly nonlinear gravity–capillary waves in the wave-frequency range $4.86 \leqslant f \leqslant 9.52\,\mathrm{Hz}$. The results of the theoretical analysis indicate that in this range of frequencies, the dissipation in the boundary layer on the free surface due to molecular viscosity has only a minor effect on the sideband wave instability. Further computations of the instability domains and the parameters of the most unstable disturbance are therefore restricted to the inviscid model only.

Gravity–capillary waves in the selected range of wave frequencies include a domain in which these waves are stable to sideband disturbances, as follows from the analysis based on the NLS equation (Djordjevic & Redekopp 1977). The present theoretical study employs the Zakharov model equation, which is free of the narrow-band approximation of the NLS equation. The results of the stability analysis of gravity–capillary waves based on the Zakharov equation are in agreement with the conclusions of Djordjevic & Redekopp, as long as only disturbances which satisfy the narrow-band approximation are considered. The present numerical study confirmed the existence of a range of gravity–capillary waves that are essentially stable. It was found, however, that this range is somewhat narrower than previously assumed, and waves within the domain of stability according to the NLS-equation-based analysis may become unstable to disturbances which have wave vectors quite different from those of the carrier wave. For short gravity–capillary waves in the range of wave frequencies considered here, most unstable disturbances and the carrier wave all propagate in different directions, so that the resulting wave field is essentially three-dimensional. While the shape of the instability domain for longer gravity–capillary waves resembles that of gravity waves, for shorter wavelengths it is quite different. The gradual transition between the two distinct shapes of the instability domains occurs in the range of carrier wavelengths where the sideband instability practically vanishes.

Another peculiar feature revealed in the stability analysis based on the Zakharov equation is a non-monotonic dependence of the growth rate of the most unstable disturbances on the carrier wave amplitude. This phenomenon is more pronounced as gravity–capillary waves become shorter. The present study demonstrates that the decrease in the maximum growth rate, starting from a particular wave steepness which is determined by the carrier wave frequency, is accompanied by a 'shrinkage' of the instability domain in the wave-vector space. This 'shrinkage' is characterized by detachment of the boundaries of the instability domain from the carrier wave frequency. The assumption of a narrow spectrum thus does not hold for these conditions.

The experiments performed in the present study confirm these theoretical conclusions qualitatively as well as quantitatively. The domains of instability for the high-frequency and the low-frequency sideband disturbances, determined experimen-

https://doi.org/10.1017/S0022112098003620 Published online by Cambridge University Press

tally from measurements of the spectra of the surface elevation performed along the propagation direction of the carrier wave, agree well with the model computations for all values of wave frequency and steepness. Moreover, experiments performed for low frequencies of the forced disturbance indeed revealed an essentially three-dimensional wave field, again in agreement with the theory. It should be mentioned here that somewhat ambiguous results were obtained for the wave frequency $f = 6.78\,\mathrm{Hz}$ ($\lambda = 4.0\,\mathrm{cm}$), where no clearly defined 'shrinkage' of the instability domain with the carrier wave steepness, as predicted by the theoretical model, could be observed in experiments.

In summary, it can thus be concluded that the Zakharov equation, which is not subject to the narrow-band approximation, represents a convenient model for studying three-dimensional surface waves. When applied to the study of the linear stability of weakly nonlinear gravity–capillary waves, it illuminates important new details of instability patterns. The corresponding experimental investigation demonstrates the accuracy of the conclusions based on the application of the Zakharov equation.

We thank Dr Chapman for his help with the capacitance wave gauges. This work was supported in part by a grant from the Israel Science Foundation.

REFERENCES

Benjamin, T. B. 1967 Instability of periodic wavetrains in nonlinear dispersive systems. *Proc. R. Soc. Lond.* A **299**, 59–75.

Benjamin, T. B. & Feir, J. E. 1967 The disintegration of wavetrains on deep water. *J. Fluid Mech.* **27**, 417–430.

Chamesse, M. 1997 An experimental study of the gravity–capillary wave field in a tank. PhD Thesis, Tel-Aviv University.

Chapman, R. & Monaldo, F. M. 1995 A novel wave height sensor. *J. Atmos. Ocean. Tech.* **12**, 190–195.

Chow, C. C., Henderson, D. & Segur, H. 1996 A generalized stability criterion for resonant triad interactions. *J. Fluid Mech.* **319**, 67–76.

Crapper, G. D. 1984 *Introduction to Water Waves*. Ellis Horwood.

Crawford, D. R., Lake, B. M., Saffman, P. G. & Yuen, H. C. 1981 Stability of weakly nonlinear deep-water waves in two and three dimensions. *J. Fluid Mech.* **105**, 177–191.

Djordjevic, V. D. & Redekopp, L. G. 1977 On two-dimensional packets of capillary-gravity waves. *J. Fluid Mech.* **79**, 703–714.

Dysthe, K. B. 1979 Note on a modification to the nonlinear Schrodinger equation for application to deep water waves. *Proc. R. Soc. Lond.* A **369**, 105–114.

Glozman, M. 1994 Energy transfer in water-waves. DSc Thesis, Technion, Haifa, Israel.

Gruman, I. 1987 Interactions of gravity–capillary wave trains. MSc Thesis, Technion, Haifa (in Hebrew).

Hasselmann, K., Raney, R. K., Plant, W. J., Alpers, W., Shuchman, R. A., Lyzenga, D. R., Rufenach, C. L. & Tucker, M. J. 1985 Theory of synthetic aperture radar ocean imaging: a MARSEN view. *J. Geophys. Res.* **90**, 4659–4686.

Henderson, D. & Hammack, J. 1987 Experiments on ripple instabilities. Part 1. Resonant triads. *J. Fluid Mech.* **184**, 15–41.

Kit, E. & Shemer, L. 1989*a* Long-time evolution and regions of existence of parametrically excited nonlinear cross-waves in a tank. *J. Fluid Mech.* **209**, 249–263.

Kit, E. & Shemer, L. 1989*b* On dissipation coefficients in a rectangular wave tank. *Acta Mech.* **77**, 171–180.

Krasitskii, V. P. 1994 On the reduced equations in the Hamiltonian theory of weakly nonlinear surface waves. *J. Fluid Mech.* **272**, 1–20.

Krasitskii, V. P. & Kalmykov, V. A. 1993 Four-wave reduced equations for surface gravity waves. *Izv. Atmos. Ocean. Phys.* **29**, 222–228.

https://doi.org/10.1017/S0022112098003620 Published online by Cambridge University Press

Lake, B. M. & Yuen, H. C. 1977 A note on some nonlinear water-wave experiments and the comparison of data with theory. *J. Fluid Mech.* **83**, 75–81.

Lighthill, M. J. 1965 Contributions to the theory of waves in non-linear dispersive systems *J. Inst. Math. Applics.* **1**, 269–306.

Longuet-Higgins, M. S. 1992 Theory of weakly damped Stokes waves: a new formulation and its physical interpretation. *J. Fluid Mech.* **235**, 319–324.

Longuet-Higgins, M. S. 1995 Parasitic capillary waves: a direct calculation. *J. Fluid Mech.* **301**, 79–107.

McGoldrick, L. F. 1965 Resonant interactions among capillary–gravity waves. *J. Fluid Mech.* **21**, 305–331.

McGoldrick, L. F., Phillips, O. M., Huang, N. E. & Hodgson, T. H. 1966 Measurements of third-order resonant wave interactions. *J. Fluid Mech.* **25**, 437–456.

McLean, J. W. 1982 Instabilities of finite-amplitude water waves. *J. Fluid Mech.* **114**, 315–330.

McLean, J. W., Ma, Y. C., Martin, D. U., Saffman, P. G. & Yuen, H. C. 1981 A new type of three-dimensional instability of finite amplitude gravity waves. *Phys. Rev. Lett.* **46**, 817–820

Melville, W. K. 1982 The instability and breaking of deep-water waves. *J. Fluid Mech.* **115**, 165–185.

Melville, W. K. 1983 Wave modulation and breakdown. *J. Fluid Mech.* **128**, 489–506.

Perlin, M. & Hammack, J. 1991 Experiments on ripple instabilities. Part 3. Resonant quartets of the Benjamin-Feir type. *J. Fluid Mech.* **229**, 229–268.

Perlin, M., Henderson, D. & Hammack, J. 1990 Experiments on ripple instabilities. Part 2. Selective amplification of resonant triads. *J. Fluid Mech.* **219**, 51–80.

Ruvinski, K. D., Feldstein, F. I. & Freidman, G. I. 1986 Effect of nonlinear damping, associated with the generation of capillary-gravity ripples, on the stability of short wind waves and their modulation by a train of internal waves. *Izv. Atmos. Ocean. Phys.* **22**, 219–224

Ruvinski, K. D., Feldstein, F. I. & Freidman, G. I. 1991 Numerical simulations of the quasi-stationary stage of ripple excitation by steep gravity-capillary waves. *J. Fluid Mech.* **230**, 339–353.

Shemer, L., Kit, E. & Miloh, T. 1987 Measurements of two- and three-dimensional waves in a channel, including the vicinity of cut-off frequencies. *Exps. Fluids* **5**, 66–72.

Shemer, L. & Marom, M. 1993 Estimates of ocean coherence time by an interferometric SAR. *Int J. Remote Sens.* **14**, 3021–3029.

Shemer, L. & Stiassnie, M. 1985 Initial instability and long-time evolution of Stokes waves. In *The Ocean Surface: Wave breaking, Turbulent Mixing and Radio Probing* (ed. Y. Toba & H. Mitsuyasu), pp. 51–57. D. Reidel.

Stiassnie, M. & Shemer, L. 1984 On modification of the Zakharov equation for surface gravity waves *J. Fluid Mech.* **143**, 229–312.

Sturm, G. V. & Sorell, F. Y. 1973 Optical wave measurement technique and experimental comparison with conventional wave height probes. *Appl. Opt.* **12**, 1928–1933.

Su, M.-Y., Bergin, M., Marler, P. & Myrick, R. 1982 Experiments on nonlinear instabilities and evolution of steep gravity-wave trains. *J. Fluid Mech.* **124**, 45–72.

Tucker, M. J. 1985 The imaging of waves by satellite borne synthetic aperture radar: the effects of sea-surface motion. *Intl J. Remote Sens.* **6**, 1059–1074.

Yuen, H. C. & Lake, B. M. 1982 Nonlinear dynamics of deep-water gravity waves. *Ann. Rev. Fluid Mech.* **22**, 67–229.

Zakharov, V. E. 1968 Stability of period waves of finite amplitude on the surface of a deep fluid. *J. Appl. Mech. Tech. Phys.* **2**, 190–194.

Zhang, J. & Melville, W. K. 1987 Three-dimensional instabilities of nonlinear gravity–capillary waves. *J. Fluid Mech.* **174**, 187–208.

https://doi.org/10.1017/S0022112098003620 Published online by Cambridge University Press